



**HAL**  
open science

## Focal-plane $Cn_2(h)$ profiling based on single-conjugate adaptive optics compensated images

Olivier Beltramo-Martin, Carlos M. Correia, Benoît Neichel, Thierry Fusco

► **To cite this version:**

Olivier Beltramo-Martin, Carlos M. Correia, Benoît Neichel, Thierry Fusco. Focal-plane  $Cn_2(h)$  profiling based on single-conjugate adaptive optics compensated images. Monthly Notices of the Royal Astronomical Society, 2018, 481 (2), pp.2349 - 2360. 10.1093/mnras/sty2399 . hal-01936864

**HAL Id: hal-01936864**

**<https://hal.science/hal-01936864>**

Submitted on 4 May 2023

**HAL** is a multi-disciplinary open access archive for the deposit and dissemination of scientific research documents, whether they are published or not. The documents may come from teaching and research institutions in France or abroad, or from public or private research centers.

L'archive ouverte pluridisciplinaire **HAL**, est destinée au dépôt et à la diffusion de documents scientifiques de niveau recherche, publiés ou non, émanant des établissements d'enseignement et de recherche français ou étrangers, des laboratoires publics ou privés.

# Focal-plane $C_n^2(h)$ profiling based on single-conjugate adaptive optics compensated images

O. Beltramo-Martin<sup>1</sup>,<sup>1</sup>★ C. M. Correia,<sup>1</sup> B. Neichel<sup>1</sup> and T. Fusco<sup>1,2</sup>

<sup>1</sup>Aix Marseille Université, CNRS, CNES LAM, 38 rue F. Joliot-Curie, 13388 Marseille, France

<sup>2</sup>ONERA, The French Aerospace Laboratory BP. 72, F-92322 Chatillon Cedex, France

Accepted 2018 August 29. Received 2018 August 29; in original form 2018 July 2

## ABSTRACT

Knowledge of the atmospheric turbulence in the telescope line-of-sight is crucial for wide-field observations assisted by adaptive optics (AO), particularly to model how the point spread function (PSF) elongates across the field of view (FOV) owing to the anisoplanatism effect. The extraction of key astronomical parameters accounts on an accurate representation of the PSF, which call for an accurate anisoplanatism characterisation. This one is, however, a function of the  $C_n^2(h)$  profile, which is not directly accessible from single-conjugate AO telemetry. It is possible to rely on external profilers, but recent studies have highlighted discrepancies of more than 10 per cent with AO internal measurements, while we aim at better than 1 per cent accuracy for PSF modelling. In order to tackle this limitation, we present focal-plane profiling (FPP) as a  $C_n^2(h)$  profiling method that relies on post-AO focal-plane images. We demonstrate that such an approach complies with a 1 per cent level of accuracy on the  $C_n^2(h)$  estimation and establish how this accuracy varies regarding the calibration star magnitudes and their positions in the field. We highlight the fact that photometry and astrometry errors caused by PSF mis-modelling reach respectively 1 per cent and 50  $\mu\text{as}$  using FPP on a Keck baseline, with a preliminary calibration using a star of magnitude  $H = 14$  at 20 arcsec. We validate this concept using Canada's NRC–Herzberg HeNOS testbed images by comparing FPP retrieval with alternative  $C_n^2(h)$  measurements on HeNOS. The FPP approach allows the  $C_n^2(h)$  to be profiled using the SCAO systems and significantly improves the PSF characterization. Such a methodology is also ELT-size-compliant and will be extrapolated to tomographic systems in the near future.

**Key words:** atmospheric effects – instrumentation: adaptive optics – methods: analytical – methods: data analysis.

## 1 INTRODUCTION

This paper focuses on improving the adaptive optics (AO) point spread function (PSF) characterization in a wide field by retrieving the distribution of atmospheric turbulence along altitude that it depends on, referred to as the  $C_n^2(h)$  profile. We consider single-conjugate adaptive optics (SCAO) system-assisted observations. The correction provided by AO is optimal in the direction of the guide star (GS), which can be either a natural guide star (NGS) or an artificial one using a laser (LGS), but degrades across the field because of the anisoplanatism effect (Fried 1982). This latter effect results from the spatial decorrelation of the incoming electric field phase that propagates through the atmosphere. The way in which this decorrelation occurs is a direct function of the  $C_n^2(h)$  and outer-

scale profiles. As a consequence, anisoplanatism broadens the PSF and induces a spatial variation of the PSF morphology across the field.

The PSF model is one of the key limitations in the current exploitation of images of crowded-field stellar populations (Fritz et al. 2010; Yelda et al. 2010; Schödel 2010) that are affected by anisoplanatism. In order to strengthen the data-processing outcome, we propose to improve the characterization of the anisoplanatism. We have established a complete and general anisoplanatism model (Beltramo-Martin et al. 2018) as a function of the input  $C_n^2(h)$  profile. This information is, however, not accessible from the AO telemetry for SCAO systems. Dedicated instruments exist to monitor this profile (Osborn 2015; Butterley, Wilson & Sarazin 2006; Wilson 2002), but they aim to characterize the observation site in terms of atmosphere quality and do not observe in the telescope line of sight. Consequently, their estimated profiles deviate by up to at least 10 per cent (Ono et al. 2017) from AO telemetry-based

\* E-mail: [olivier.beltramo-martin@lam.fr](mailto:olivier.beltramo-martin@lam.fr)

approaches available for multi-GS AO systems (Helin et al. 2018; Guesalaga et al. 2017; Laidlaw et al. 2016; Martin et al. 2016; Neichel et al. 2014). However, according to Beltramo-Martin et al. (2018), 10 per cent of error on the  $C_n^2(h)$  estimation may degrade the photometry and astrometry determination up to respectively 3 per cent and 300  $\mu\text{as}$  in a 20-arcsec FOV, while we are seeking to reach better than 1 per cent and 150  $\mu\text{as}$ .

We propose in this paper to rely on the SCAO-compensated PSFs available across the field. We focus on SCAO systems that do not permit the identification of the  $C_n^2(h)$  from the telemetry and would benefit from having an internal image-based facility to retrieve the profile, either for post-processing or real-time application. The methodology we present can be extended to multi-GS systems, but at the cost of a greater numerical complexity to include the AO system control specificity, such as the tomographic reconstruction step or the optimal fitting in multi-conjugated AO. Before considering such systems, we will address the ground-layer AO case and compare our present approach with telemetry-based  $C_n^2(h)$  estimation.

Spatial variations of the AO PSF encode the real  $C_n^2(h)$  that affects images and the one that we want to determine. In order to extract the profile from images, we have developed the focal-plane profiling (FPP) method as a non-linear least-squares minimization procedure that adjusts a  $C_n^2(h)$ -dependent PSF model to match a collection of observations and deliver a joint estimation of the PSF model and  $C_n^2(h)$  profile. If the model is not consistent with real atmosphere statistics, because we consider a profile over too few bins for instance, the minimization process allows us to mitigate these errors when extrapolating the PSF in the field. If we feed this inaccurate model with a wrong  $C_n^2(h)$  without any feedback from a real PSF, we risk amplifying the error propagation and degrading the PSF extrapolation.

We describe the FPP algorithm in Section 2. Section 3 is dedicated to FPP performance assessment: we illustrate that the FPP allows us to retrieve the  $C_n^2(h)$  at a 1 per cent level of accuracy when bright stars are available. We present an application to PSF extrapolation on simulated images of NIRC2 (McLean & Chaffee 2000) at Keck II and evaluate the conditions in terms of the calibration star magnitudes and field locations that are required to decrease the errors caused by PSF-model indetermination on the photometry and astrometry, down to respectively 1 per cent and 50  $\mu\text{as}$ . In a further step we apply the FPP to Canada's NRC–Herzberg HeNOS testbed images and successfully compare the FPP-retrieved  $C_n^2(h)$  with existing measurements.

## 2 FOCAL-PLANE PROFILING

The full width at half-maximum (FWHM) of a seeing-limited PSF is known to be settled by atmospheric turbulence properties, such as the seeing and the outer scale. Thus, these parameters can be extracted directly from observed PSFs, as shown by Martinez et al. (2010).

In this paper, we extend this methodology to characterize the entire  $C_n^2(h)$  profile based on an AO-compensated PSF. FPP is designed to exploit anisoplanatism patterns observed on off-axis PSFs, namely not in the GS location, in order to retrieve the  $C_n^2(h)$  profile as really seen by the AO system. It relies on a PSF model (Beltramo-Martin et al. 2018) regarding angular variations across the field arising from anisoplanatism. Furthermore, the problem inversion is performed by minimising the Euclidian distance of the model to imaged PSFs in acting iteratively on the profile that describes the anisoplanatism.

### 2.1 Direct problem

Let  $\rho$ ,  $\lambda$  and  $\theta$  be respectively the coordinate vector in the pupil, the imaging wavelength and the angular position on the sky. We define  $\text{OTF}(\rho/\lambda, C_n^2(h), \theta)$  as an AO-compensated estimated optical transfer function (OTF) in the direction  $\theta$  in the field, which is derived as follows:

$$\text{OTF}(\rho/\lambda, C_n^2(h), \theta) = \text{OTF}_0(\rho/\lambda) \cdot \text{ATF}(\rho/\lambda, C_n^2(h), \theta), \quad (1)$$

where  $\text{OTF}_0$  is the OTF in the reference direction, which can be either a real observation or a model delivered by PSF reconstruction (Véran et al. 1997) for instance. In the remainder of this paper, we will assume that  $\text{OTF}_0$  is known perfectly. Then, the PSF in the field direction  $\theta$  is given by the Fourier transform of  $\text{OTF}(\rho/\lambda, C_n^2(h), \theta)$ .

ATF, which appears in equation (1), is the anisoplanatism transfer function as introduced by Fusco et al. (2000). It is derived as

$$\text{ATF}(\rho/\lambda, C_n^2(h), \theta) = \frac{\iint_{\mathcal{P}} \mathcal{P}(\mathbf{r}) \mathcal{P}(\mathbf{r} + \rho) \exp(-0.5 \times D_{\Delta}(\mathbf{r}, \rho, C_n^2(h), \theta)) \, d\mathbf{r}}{\iint_{\mathcal{P}} \mathcal{P}(\mathbf{r}) \mathcal{P}(\mathbf{r} + \rho) \, d\mathbf{r}}, \quad (2)$$

where  $\mathcal{P}$  is the pupil function,  $\mathbf{r}/\rho$  are respectively the location/separation vector in the pupil, and  $D_{\Delta}$  is the anisoplanatic phase structure function.  $D_{\Delta}(\mathbf{r}, \rho, C_n^2(h), \theta)$  characterizes the spatial decorrelation of two wavefronts coming from two stars angularly separated by  $\theta$  in the field. Through the ATF calculation in equation (2), the anisoplanatism sharpens the angular frequencies support, namely  $\text{OTF}_0$ , which elongates the PSF towards the GS direction. At a field position  $\theta$ , the PSF broadening is fully determined by  $D_{\Delta}(\mathbf{r}, \rho, C_n^2(h), \theta)$ , which is a function of the  $C_n^2(h)$  as detailed in the literature (Beltramo-Martin et al. 2018; Flicker 2008; Fusco et al. 2000; Britton 2006; Whiteley, Welsh & Roggemann 1998; Tyler 1994). Note that the ATF should not be pupil-model-dependent regarding equation (2), which introduces the normalization by the diffraction OTF. The real telescope pupil filtering is carried by  $\text{OTF}_0$ .

### 2.2 Problem inversion

Equation (2) highlights the fact that the PSF model is highly non-linear regarding the inputs. The approach to inverting the problem that we have chosen consists of iteratively least-squares minimizing the criterion given in equation (3) using a Levenberg–Marquardt algorithm. For  $n_{\text{psf}}$  observations in the field, FPP minimizes the following cost function:

$$\varepsilon^2(C_n^2(h)) = \sum_{i=1}^{n_{\text{psf}}} \left\| \left( \text{PSF}(\boldsymbol{\alpha}, \theta_i) - \widehat{\text{PSF}}(\boldsymbol{\alpha}, \theta_i, C_n^2(h)) \right) \right\|_{\mathcal{L}_2}^2, \quad (3)$$

where  $\text{PSF}(\boldsymbol{\alpha}, \theta_i)$  and  $\widehat{\text{PSF}}(\boldsymbol{\alpha}, \theta_i, C_n^2(h))$  are respectively the observed and modelled PSF in the field direction  $\theta_i$  as function of the angular separation vector  $\boldsymbol{\alpha}$  in the focal plane. Fig. 1 represents the FPP architecture as a block diagram.

The FPP algorithm starts from an initial guess on the profile, which is chosen to be flat but with an integral that corresponds to  $r_0^{-5/3}$ . This constraint is easily reached thanks to the AO telemetry that permits a  $r_0$  estimation with an accuracy of 10 per cent. FPP derives the OTF in the field directions given by the vector  $\boldsymbol{\theta}$  using equation (1), where  $\text{OTF}_0$  is an input of the problem. We then do zero-padding and interpolate the OTF and compute its Fourier transform to obtain the PSF with the desired pixel scale and FOV,

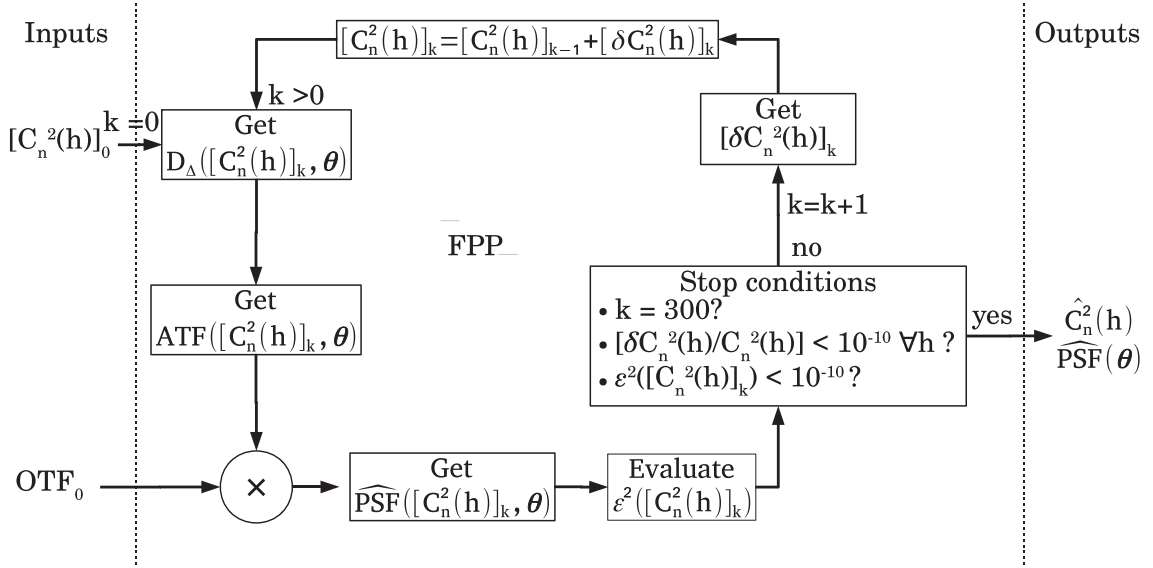


**Figure 1.** Block diagram representing the FPP architecture. The algorithm must be provided by a reference OTF ( $OTF_0$ ) and an initial guess on the  $C_n^2(h)$ . We have chosen a flat initial profile whose integral corresponds to  $r_0^{-5/3}$ .

before scaling it to set its flux to that of the observation. From the concatenation of the modelled PSFs given at any element of  $\theta$ , FPP calculates the criterion in equation (3) and evaluates whether the stop conditions are met: either the criterion or the relative increment on the  $C_n^2(h)$  reaches  $10^{-10}$  for any bin, or the iteration number meets 300, which is a reasonable empirical evaluation. In the situation in which the algorithm ought to continue going through the iterative loop, it updates the  $C_n^2(h)$  value from the empirical model gradient and updates the PSF model until reaching the stop conditions. When these are met, the FPP delivers the PSF model at any field position given by  $\theta$  and the corresponding  $C_n^2(h)$  estimation.

We could define an OTF-based criterion: we can select a Cartesian area in the PSF by applying a sinc filter to the OTF, to remove the contribution of the PSF wings for instance, which are not sensitive to the  $C_n^2(h)$  distribution but only to the integrated value. However, the anisoplanatism enlarges the PSF and sharpens the OTF. Consequently, a strong anisoplanatism effect narrows the OTF and decreases the number of useful pixels to be model-fitted, which yields a sensitivity loss to  $C_n^2(h)$ . In addition, an OTF-based fitting would potentially allow us to deal more efficiently with white noise, but the processing of NIRC2 images, on which we will test the method, has shown that the noise can be spatially correlated and contaminates more than the central OTF pixel. It is thus not necessarily straightforward to mitigate the noise contribution in an OTF-based criterion with spatially correlated noise. So far, the PSF-based criterion appears to be more convenient in a first implementation of the method and also more intelligible for the community of potential users, but we plan to improve the FPP robustness and efficiency in the future. In particular, we will determine whether an OTF-based criterion may help us in relation to this goal.

As illustrated by equation (3), FPP bases on pixel intensity variations in the focal plane and more particularly on a feature that is spatially correlated. When the PSF is off-axis, a large part of this spatial variation is induced by anisoplanatism, as illustrated in Fig. 2. We could potentially rely only on the FWHM value to estimate the original  $C_n^2(h)$  that explains the PSF broadening, but we see several problems with this approach. First, the PSF FWHM varies very little regarding  $\theta$  as long as  $\theta$  is lower than  $1.5 \theta_0$ . Con-

sequently a large field, basically 30 arcsec in the  $H$  band, would be required for a linear dependence between the FWHM and the  $C_n^2(h)$  value, which could be larger than the imager FOV. Furthermore, the FWHM is only a scalar value and we need to retrieve the  $C_n^2(h)$  value over several bins, at least seven as noted in Beltramo-Martin et al. (2018); we would therefore need at least seven PSFs in different positions in the field to expect a full profile retrieval, which would be challenging. The use of all the PSF pixels within the AO control radius ensures that we theoretically have enough sensitivity to extract the profile from a single PSF.

### 3 METHOD SENSITIVITY AND PERFORMANCE

We have simulated a grid of PSFs in Fig. 2 using the wavefront propagation object-oriented code OOMAO (Conan & Correia 2014). Atmosphere set-up refers to Mauna Kea median conditions, and the telescope and AO characteristics follow a Keck II baseline as detailed in Table 1. We did not simulate a real AO system: we assumed that the on-axis PSF is diffraction-limited and defined by a circular pupil only. We want to determine the potential of the FPP method in such a limited case before applying it to real AO sky data. More generally, FPP does not need any assumption about the AO system because of our knowledge of  $OTF_0$ , which contains information on exactly what the AO system has done. It only requires the atmospheric turbulence distribution that makes the PSF vary across the field. In other words, simulating a real on-axis PSF would not really change the results below, because we assume that  $OTF_0$  is known perfectly. The case in which we do not make this assumption and use PSF reconstruction to identify  $OTF_0$  is treated in another publication.

In the following, we compare the FPP  $C_n^2(h)$  retrieval in relation to the calibration star magnitudes and numbers. The term calibration will refer to the  $C_n^2(h)$  estimation using FPP that performs this calibration. For instance, *calibration stars* refers to the specific stars in the field whose PSF is provided to FPP to identify  $C_n^2(h)$ . Simulated PSFs are distributed along concentric rings of 5 arcsec up to a 40-arcsec zenith angle (ZA), as represented in Fig. 3. In

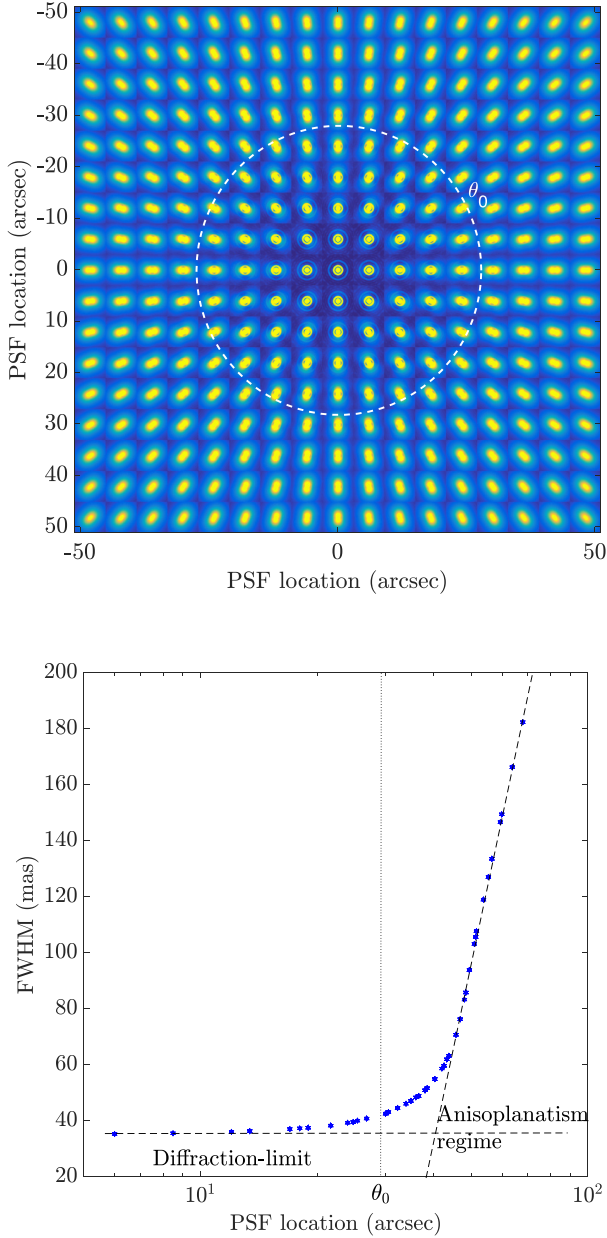


**Figure 2.** (Top) Adaptive optics-compensated point spread functions (PSFs) across the field. Ticks give the corresponding PSF location from the guide star direction. (Bottom) Full width at half-maximum as a function of field position from on-axis.

Section 3.1, we assess the limit on the calibration field position to ensure a full  $C_n^2(h)$  retrieval. In Section 3.2, we analyse how the noise that contaminates calibration PSFs propagates into the  $C_n^2(h)$  retrieval process. To do this, we extract calibration PSFs from 40- to 20-arcsec ZA to feed the FPP. In order to increase the amount of non-redundant information and the overall signal-to-noise ratio (SNR), we concatenated these PSFs from the farthest to the closest; that is, in equation (3),  $i = 1$  refers to the 40-arcsec-ZA star. As long as the calibration PSF is located beyond  $\theta_0$ , we have verified that the FPP estimates perfectly the entire profile using this PSF; that is, there is no specific gain by relying only on the 20- or the 40-arcsec-ZA star, at least for noise-free images. When introducing noise, the 40-arcsec-ZA star is more elongated and its energy is

**Table 1.** Simulation set-up summary based on a Mauna Kea median profile. Note that the anisoplanatism only occurs on bin layers strictly above 0 km.

Sources wavelength [ $\mu\text{m}$ ]	1.65
Exposure time [s]	30
Zero point [ $\text{mag s}^{-1}$ ]	25.5
$r_0$ [nm] (500 nm)	0.16
$L_0$ [m]	25
$\theta_0$ (1.65 $\mu\text{m}$ ) [arcsec]	22
fractional $r_0$ [%]	51.7, 11.9, 6.3, 6.1, 10.5, 8.1, 5.4
altitude layer [km]	0, 0.5, 1, 2, 4, 8, 16
Telescope diameter [m]	10
Telescope elevation [deg]	30
# pixels in the pupil	200
DM actuator pitch [m]	0.5
WFS # lenslets	20

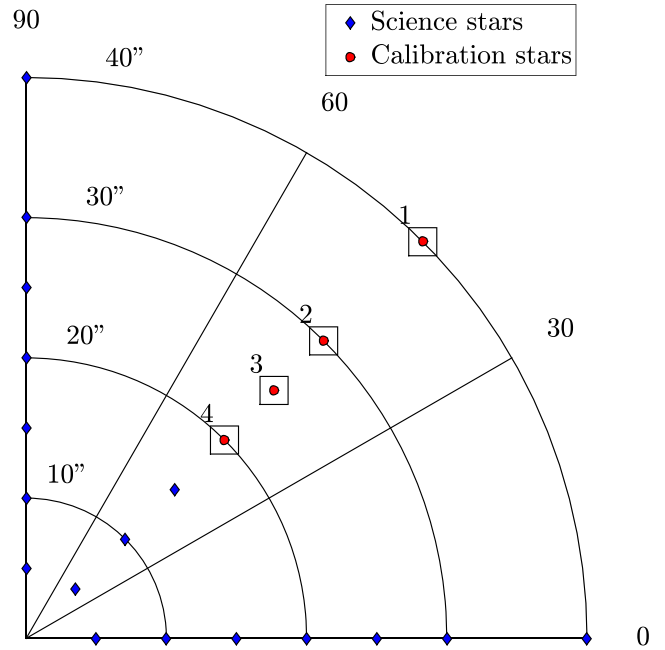


**Figure 3.** Spatial distribution of simulated sources in the (azimuth angle, zenith angle) plane. Circles refer to calibration star positions, where the FPP takes the reference PSFs, in a sequence labelled from 1 to 4, to calibrate the  $C_n^2(h)$  profile.

spread over the focal plane and it is therefore more contaminated by the Poisson noise. By changing the reference star position from the 40- to the 20-arcsec-ZA, we progressively increase the overall SNR.

Star magnitudes are set up by scaling the PSF flux with regard to the  $H$ -band zero-point value of  $25.5 \text{ mag s}^{-1}$  for the NIRC2 detector at Keck II. We consider photon noise and 38 counts by pixel for the read-out noise and  $0.08 \text{ count pixel}^{-1} \text{ s}^{-1}$  for the dark current. Sky background is included as well and set to  $13.6 \text{ mag arcsec}^{-2} \text{ s}^{-1}$  in the  $H$  band.

Finally, in all the following, both the simulation and the FPP model have the same altitude-resolution capability; that is, we configured the FPP to retrieve six layers in altitude. The impact of altitude distribution errors is discussed in Beltramo-Martin et al. (2018). Because we assume that we know  $\text{OTF}_0$ , the ground-layer fraction at 0 km does not contribute to the anisoplanatism and cannot be identified by FPP. In a future publication we will present an

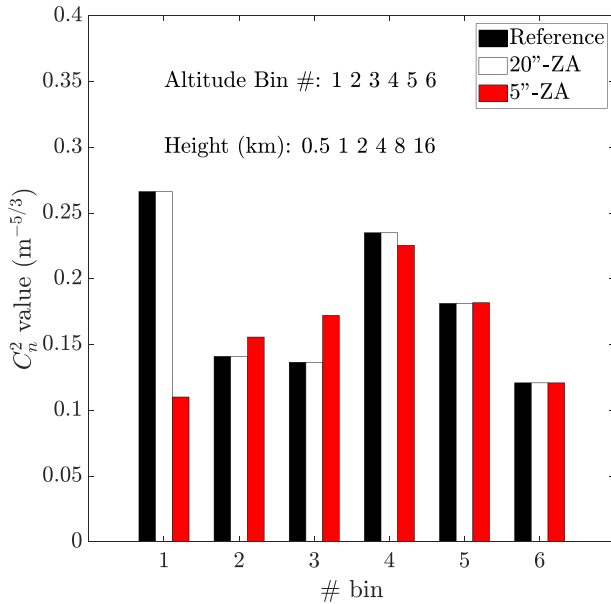


**Figure 4.** Retrieved  $C_n^2(h)$  profile using a single point spread function located either at 5- or 20-arcsec ZA.

extension to FPP in order to estimate the ground-layer contribution by adjusting the PSF wings.

### 3.1 Sensitivity to anisoplanatism strength

We consider that the atmosphere bin heights are perfectly known. We first address the question of FPP sensitivity: how large must the FOV be for having an anisoplanatism effect sufficiently strong to be perfectly characterised by the FPP? The closest PSFs are less contaminated by anisoplanatism, as illustrated in Fig. 2; that is, there are fewer pixels that the FPP can rely on to perform the retrieval. We thus expect that there exists a threshold on  $\theta$  below which the FPP cannot identify the entire profile accurately.

In order to determine the existence of this threshold, we ran the FPP algorithm to retrieve  $C_n^2(h)$  using a single simulated PSF located between 1 and 40 arcsec from the GS position. Fig. 4(a) shows a comparison of estimated  $C_n^2(h)$  regarding the PSF location. It can be seen that the profile is perfectly identified as long as the PSF is sufficiently affected by the anisoplanatism.

The presence of this threshold is confirmed by Fig. 5, which shows the accuracy on bin strengths regarding the calibration star position. The figure clearly highlights that the entire profile is retrieved as long as  $\theta > (2/3)\theta_0$ . Below this threshold, bins at the lowest altitude are not well retrieved, with a clear trend of accuracy degradation for reference PSFs closer to on-axis and lower altitudes. We note that the accuracy improvement is not linear with respect to  $\theta$ , but resembles a succession of plateaus. We believe that this is a result of the particular Mauna Kea median profile that we used to perform this study; if we took another one we would have a different shape, but still the same level of mean error and a strong breakout at  $\theta = (2/3)\theta_0$ , such that the main conclusion of our analysis remains the same.

Fig. 5 also gives the number of layers that we can reconstruct with regard to the location we pick off the PSF. For instance, to obtain a 1 per cent of accuracy on  $C_n^2(h)$  using a 10-arcsec-ZA PSF, we can only reconstruct the three highest layers, a number that is reduced to two for a 5-arcsec-ZA PSF. In other words, in the case

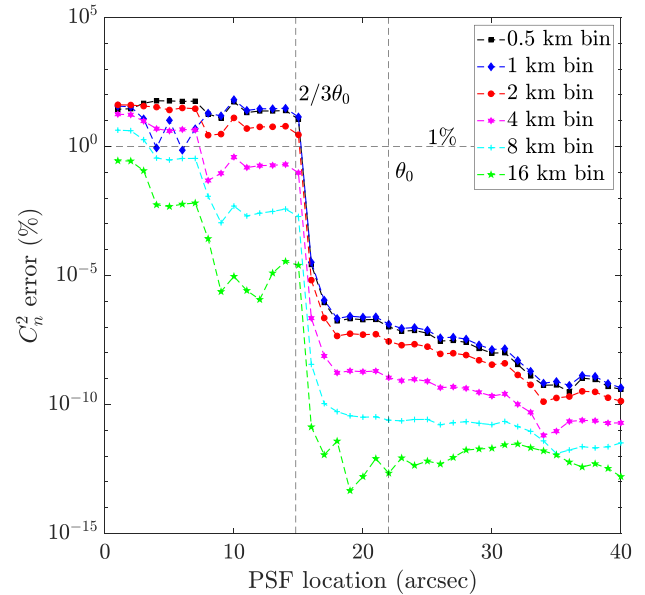


**Figure 5.** Accuracy on  $C_n^2(h)$  bins regarding the calibration point spread function location that is provided to the focal-plane profiling.

**Table 2.** Isoplanatic angle values at  $1.65 \mu\text{m}$  regarding the  $r_0$  zenith value at 500 nm at Mauna Kea and the telescope elevation. The outer scale was fixed to 25 m.

	Telescope elevation [deg]				
$r_0$ at 500 nm [cm]	0	15	30	45	60
8	12.1	11.4	9.5	6.7	3.8
12	19.8	18.6	15.0	10.9	6.0
16	28.6	26.9	22.0	15.5	8.5
18	33.5	31.4	26.1	18.0	9.8
20	38.7	36.3	30.2	20.6	11.2

of a 10-arcsec FOV, as for the narrow-field mode of NIRC2, a PSF model based on three altitude layers is sufficient to characterize its properties at an accuracy of 1 per cent.

In Table 2 we report the isoplanatic angle value as function of the  $r_0$  value at zenith and the telescope elevation for an outer scale of 25 m. Considering that we need a PSF positioned at  $\theta_0$  off-axis, the table tells us where we must pick-off an observation to ensure the full  $C_n^2(h)$  retrieval at 1 per cent accuracy. For instance, for median conditions ( $r_0 = 16$  cm), we would need an observation at 22 arcsec to retrieve seven layers for  $30^\circ$  of telescope elevation.

### 3.2 Sensitivity to noise

We now consider the 40-arcsec-field case (NIRC2, wide-field mode), with the atmosphere/telescope set-up as detailed in Table 1. We discuss how noise propagation affects the  $C_n^2(h)$  retrieval.

We continue to consider simulated images, which are now noise-contaminated following a NIRC2 baseline. As we saw previously, these PSFs are affected enough by anisoplanatism to permit a full profile retrieval over the seven layers.

The FPP algorithm is tested for a collection of PSFs whose magnitude (the same for each star) varied from  $H = 10$  to 17. We report in Fig. 6 the FPP-estimated  $\theta_0$  as a function of the calibration star magnitudes and numbers. The figure illustrates that the noise that

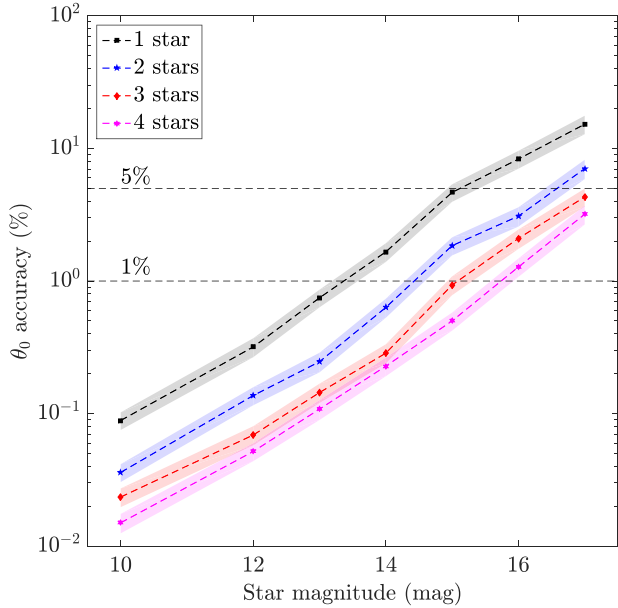


**Figure 6.** *H*-band isoplanatic angle  $\theta_0$  accuracy as a function of the focal-plane profiling calibration star magnitudes. Envelopes are for a  $1\sigma$  standard deviation.

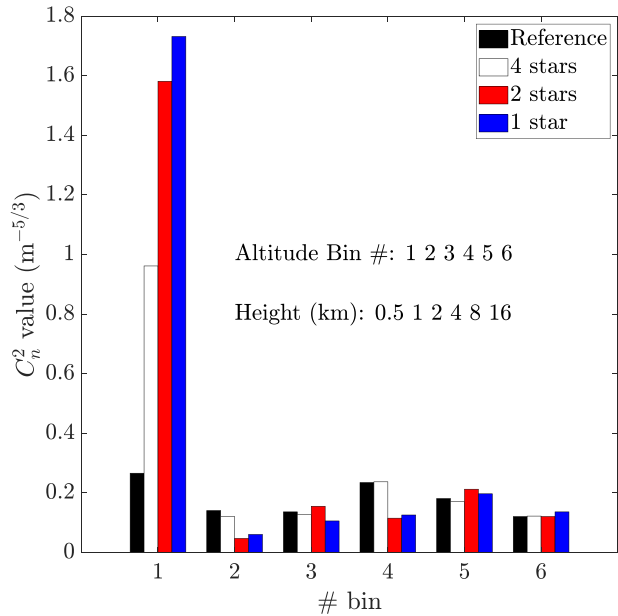


**Figure 7.** Retrieved  $C_n^2(h)$  profile as a function of the number of collected point spread functions for calibration star magnitudes set to 15.

contaminates the calibration PSF propagates through the minimization process and degrades the  $C_n^2(h)$  retrieval. This contamination can be mitigated by relying on more calibration PSFs, which improves the overall SNR and the  $C_n^2(h)$  accuracy. An level of accuracy of approximately 1 per cent on  $\theta_0$  is obtained with a single star of magnitude 13.5.

Figs 7 and 8 report the FPP-estimated  $C_n^2(h)$  profile compared with the simulation reference, for different numbers of collected PSFs and different magnitude levels. As previously, the results confirm that increasing the number of calibration stars helps the identification. Furthermore, the lowest bins are the most sensitive

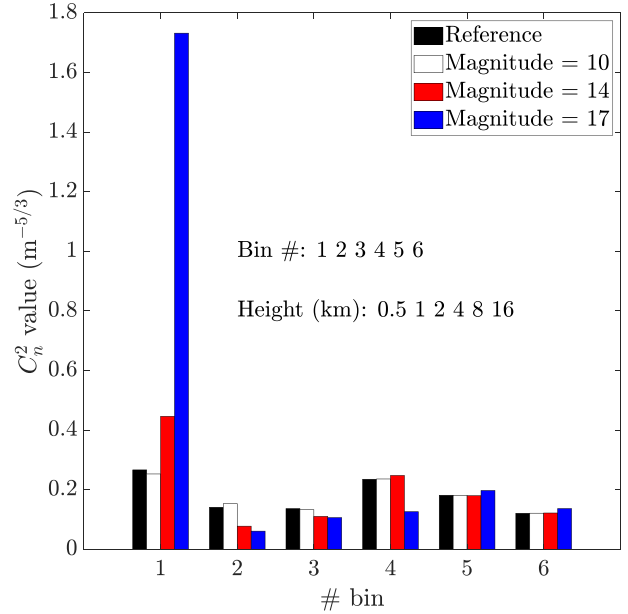


**Figure 8.** Retrieved  $C_n^2(h)$  profile with respect to calibration star magnitudes when picking off four point spread functions in the field.

to the noise level; they are the ones that contribute the least to the anisoplanatism effect, as discussed in Section 3.1. The degradation of  $\theta_0$  is consequently mostly explained by inaccuracies on these lowest layers.

In conclusion, in order to provide a  $C_n^2(h)$  profile estimation that reaches 1 per cent accuracy on  $\theta_0$  using *H*-band NIRC2 images, the FPP needs to rely on a single star of magnitude  $H = 13.5$ , located at least beyond  $(2/3)\theta_0$ . We expand this quantitative constraint of the FPP as a function of the exposition time and number of calibration stars in Section 4.3.

#### 4 APPLICATION TO PSF EXTRAPOLATION

We continue handling noise-contaminated NIRC2 simulated images in order to assess the accuracy we can expect on PSF properties by using the FPP. As previously, we extracted several stars in an anisoplanatism-limited area, with noise contamination, to calibrate the PSF model across the field. Modelled PSFs are compared with simulations in terms of the Strehl ratio (SR) and FWHM.

In addition, we aim to quantify astronomical metrics, such as photometry and astrometry. We used the same baseline as presented in Beltramo-Martin et al. (2018) for tight binaries. For each simulated star, we created a corresponding 100-mas-separated simulated binary by duplicating and shifting the PSF. The purpose of this manipulation was to measure how well we can retrieve the binary characteristics by fitting a model provided by the FPP. Basically, photometry and astrometry are measured from the residual of the PSF scaling and relative position adjustments over the synthetic binary, when using a binary model based on the FPP PSF model that may differ from the real simulated PSF. The process is repeated for any value of  $\theta$ . Because the FPP relies on noisy calibration PSFs, we aim here to assess how the noise impacts the binary parameter estimation by biasing the PSF-model representation that we calibrate using the FPP. We summarize the methodology in Fig. 9.

For each considered metric, we looked either at its mean value across the field regarding the calibration star magnitudes, or at how it varies with angular separation from on-axis.

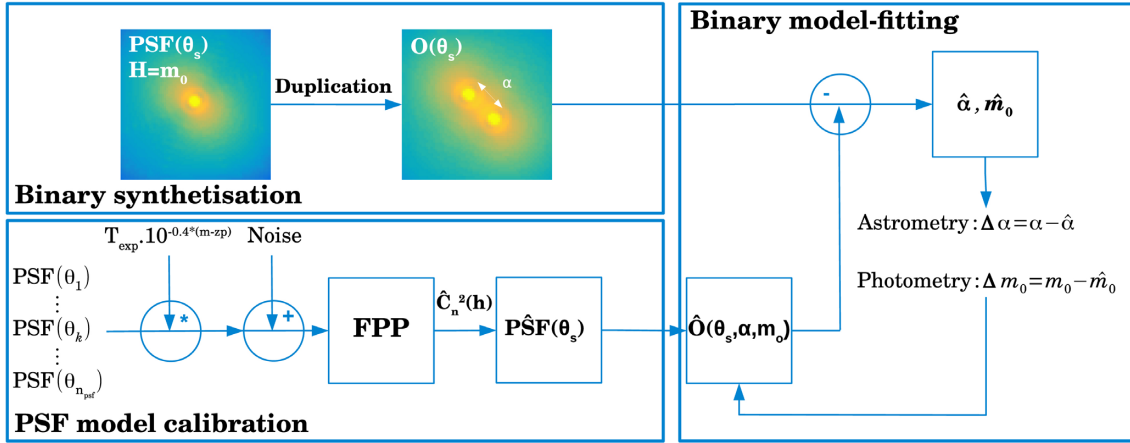


**Figure 9.** Sketch of the binary parameter retrieval. For each field location  $\theta_s$ , we create a fake binary with a known separation  $\alpha$  and magnitude  $m_0$ . In parallel, we calibrate the PSF model using the FPP over a collection of noise-contaminated calibration PSFs of magnitude  $m$ , with  $zp$  the zero-point and  $T_{\text{exp}}$  the exposure time. This model is duplicated to create a binary model as a function of the stars' fluxes and relative separation, which is adjusted iteratively over the synthetic observation.

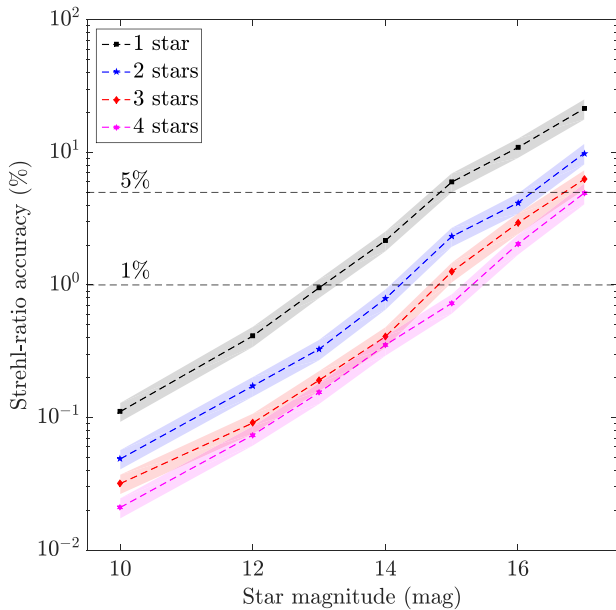


**Figure 10.**  $H$ -band Strehl ratio accuracy averaged out over the field in relation to the calibration star magnitudes. Envelopes are for a  $1\sigma$  standard deviation.

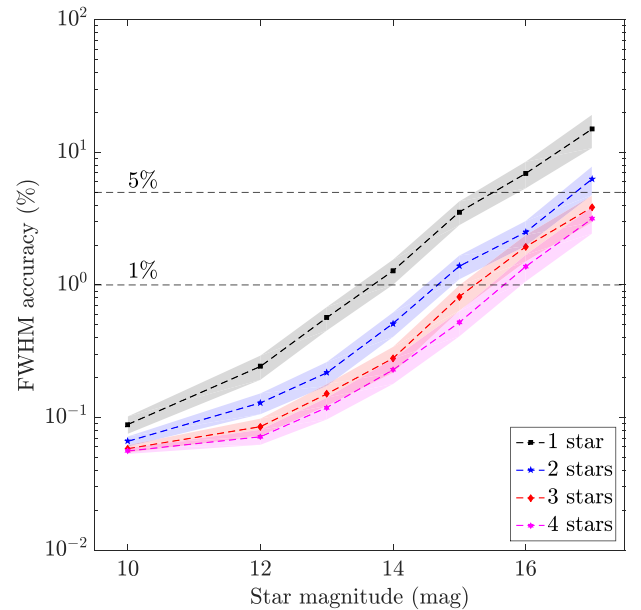


**Figure 11.**  $H$ -band full width at half-maximum accuracy averaged out over the field in relation to the calibration star magnitudes. Envelopes are for a  $1\sigma$  standard deviation.

#### 4.1 Impact on PSF morphology

The SR and FWHM are known (Roddier 1999) to follow  $\theta_0$ -dependent laws given respectively by  $\exp(\theta_0^{-5/3})$  and  $(\theta/\theta_0)^{-5/3}$ . We expect to retrieve trends connected to what is presented in Fig. 6.

Figs 10 and 11 display the SR and FWHM mean accuracy in the field with regard to the calibration star magnitudes. We retrieved similar linear trends with respect to  $\theta_0$  as presented in Fig. 6, which confirms that the accuracy of these parameters is related to  $\theta_0$  estimation errors regarding the noise level.

Figs 12 and 13 show the SR and FWHM accuracy as a function of  $\theta$  when calibrating the  $C_n^2(h)$  profile with one to four stars of magnitude 15. When relying on more stars, the  $C_n^2(h)$  estimation is better, as seen in Section 3.2, which translates into a better PSF modelling downstream.

The model accuracy is not, however, uniform across the field. The PSFs that are closest to from on-axis are less affected by anisoplanatism; that is, the PSFs at these positions are not sensitive to any  $C_n^2(h)$  mis-retrieval, which explains why the SR and FWHM values are better estimated for smaller separations. For farthest separations, the PSF model is calibrated using at least the 40-arcsec-ZA star; consequently, the PSF must be well characterized at this specific location for the single-calibration PSF case, which justifies why we see this drop in error for the 40-arcsec separation. By gathering up more calibration stars from 40- to 20-arcsec ZA, in addition to improving the PSF morphology characterization, we make the estimates more uniform across the field.

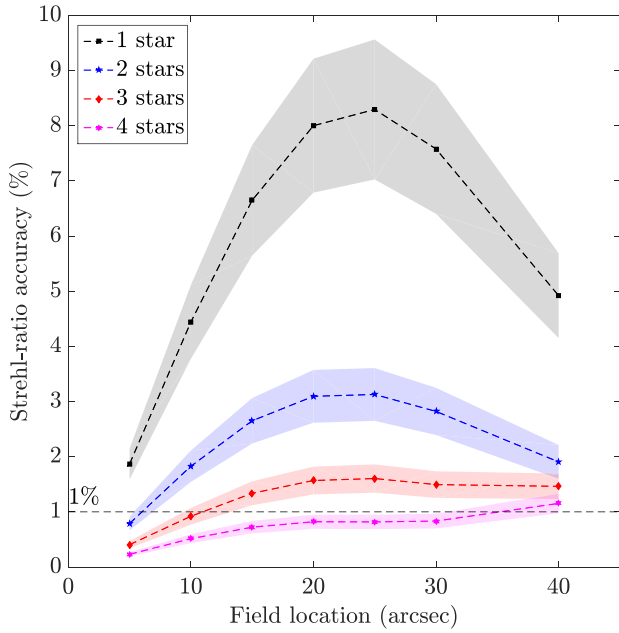


**Figure 12.** *H*-band Strehl ratio accuracy in the field in relation to the number of calibration stars of magnitude 15. Envelopes are for a  $1\sigma$  standard deviation.

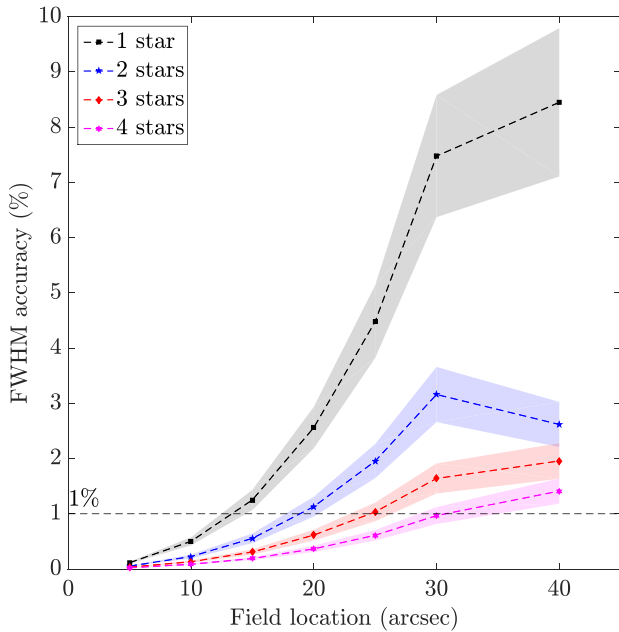


**Figure 13.** *H*-band full width at half-maximum accuracy in the field in relation to the number of calibration stars of magnitude 15. Envelopes are for a  $1\sigma$  standard deviation.

#### 4.2 Impact on binary photometry and astrometry

Figs 16 and 17 show, respectively, the photometry and astrometry with respect to the PSF location in the field. As for PSF-related metrics, photometry and astrometry are not estimated uniformly, for the reasons given in Section 4.1. Figs 14 and 15 show the same linear trends on photometry and astrometry estimates errors with respect to the calibration star magnitudes.

We observe that the photometry and astrometry accuracy are respectively connected to the SR and FWHM estimation, as expected

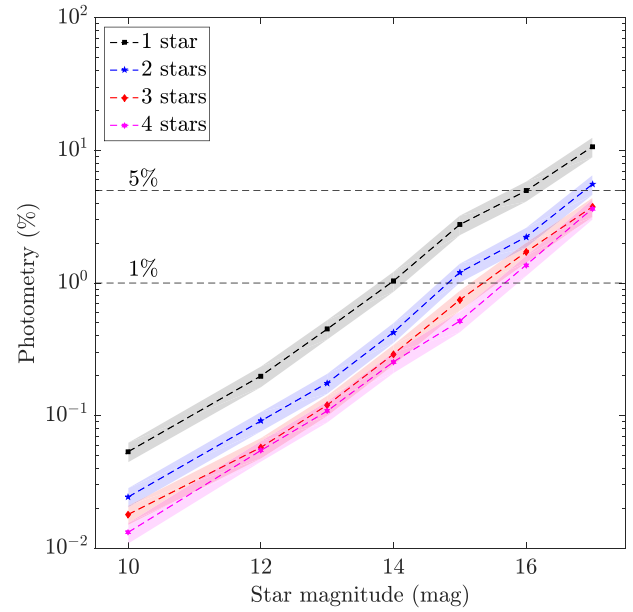


**Figure 14.** *H*-band photometry accuracy averaged out over the field in relation to the calibration star magnitudes. Envelopes are for a  $1\sigma$  standard deviation.

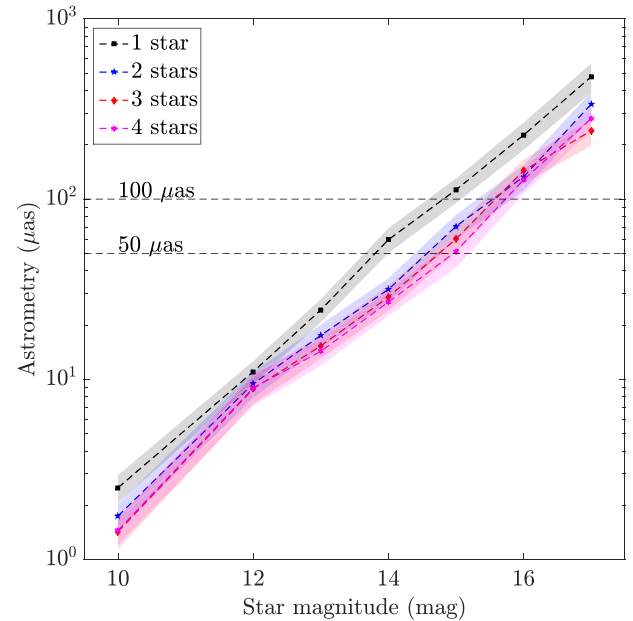


**Figure 15.** *H*-band astrometry accuracy averaged out over the field in relation to the calibration star magnitudes. Envelopes are for a  $1\sigma$  standard deviation.

(Beltramo-Martin et al. 2018). For a single calibration star of magnitude 14, we obtain a 1 per cent level for photometry and  $50 \mu\text{as}$  for astrometry. These values reflect only PSF model errors onto the estimates; we do not consider any other potential effects that contribute to the overall error, as detailed in Fritz et al. (2010) for astrometry in the Galactic Centre for instance, which explains why the astrometry drops to zero for stars close to the GS: in the absence of anisoplanatism, we do not propagate any  $C_n^2(h)$  mis-retrieval into the PSF model.

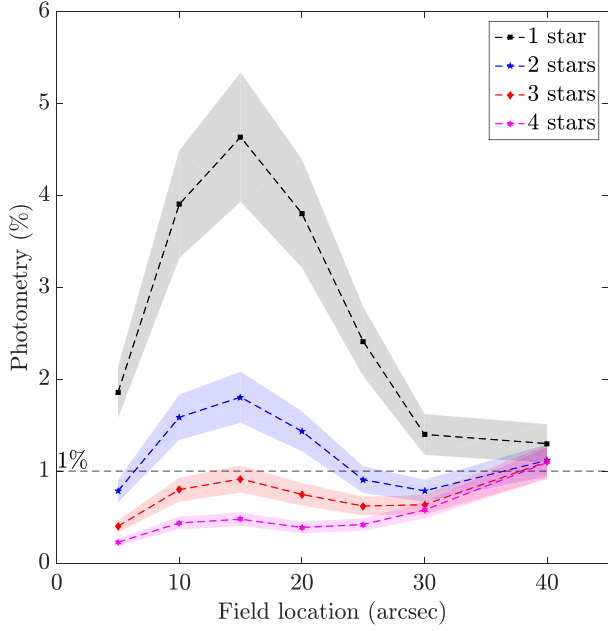


**Figure 16.** *H*-band photometry accuracy in the field in relation to the number of calibration stars of magnitude 15. Envelopes are for a  $1\sigma$  standard deviation.

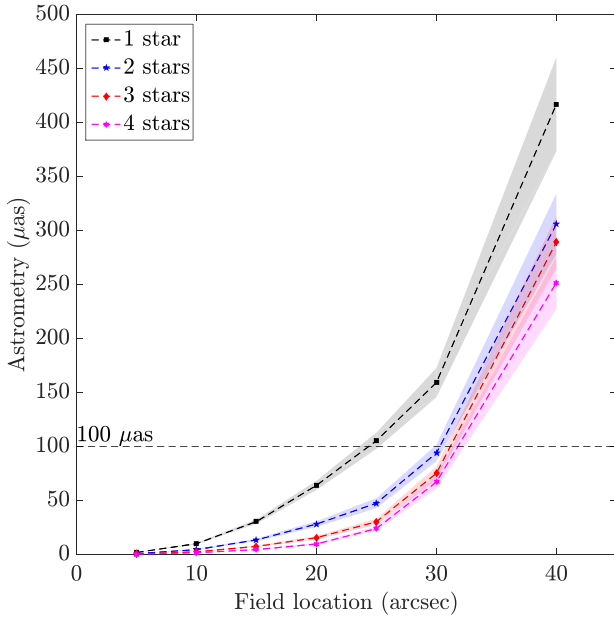


**Figure 17.** *H*-band astrometry accuracy in the field in relation to the number of calibration stars of magnitude 15. Envelopes are for a  $1\sigma$  standard deviation.

In contrast to the case for photometry, astrometry behaves as a monotonic function of the field location. This reflects the fact that the astrometry is roughly given by the ratio FWHM/SNR and so is sensitive to the slope of the averaged PSF core. Because the PSF FWHM increases monotonically as a function of  $\theta$ , as shown in Fig. 2, we retrieve the same behaviour for the astrometry versus  $\theta$ , where the function increases less rapidly if we increase the SNR by calibrating the PSF model over more stars.

One may argue that more efficient and robust tools exist to estimate the photometry and astrometry. However, our purpose is only

**Table 3.** *H*-band star magnitude limits regarding the number of stars and exposure time to obtain a 1 per cent accuracy on photometry within a  $40 \text{ arcsec} \times 40 \text{ arcsec}$  field of view using NIRC2 at Keck II.

$n_{\text{psf}}$	$T_{\text{exp}}$ [s]				
	1	10	30	60	120
1	10.3	12.8	14	14.7	15.5
2	11.0	13.6	14.7	15.5	16.3
3	11.5	14.0	15.2	15.9	16.7
4	11.8	14.3	15.5	16.3	17.0
5	12.0	14.6	15.7	16.5	17.2

to focus on PSF model error contributions resulting from bad anisoplanatism characterization, which can be assessed regardless such algorithms. We highlight that we can mitigate mis-knowledge of anisoplanatism and reach as low as  $50 \mu\text{as}$  and 1 per cent, respectively, for astrometry and photometry over  $40 \text{ arcsec}$  when calibrating the FPP using a single star. In the near future, we will apply FPP to real crowded field observations and use a standard pipeline to assess the potential gain on estimates.

### 4.3 Threshold values

We use our previous analyses to determine which configuration permits a 1 per cent accuracy estimation of a given metric. We perform the exercise for photometry, but the same methodology is applicable for any other metrics, as long as we have identified how it varies with regard to the SNR.

According to Fig. 14, a 1 per cent accuracy on photometry in the field requires us to calibrate the FPP model using a single  $m_0 = 14$ -mag PSF imaged with a 30-s exposure time. For a different star magnitude, exposure time and number of collected images, we must ensure that the total gathered flux corresponds to a 14-mag star. If  $m_*(n_{\text{psf}}, T_{\text{exp}})$  is the magnitude limit over the  $n_{\text{psf}}$  we obtain from the field and is imaged at  $T_{\text{exp}}$  s of exposure time, it must satisfy

$$-2.5 \log_{10} \left( \frac{n_{\text{psf}} T_{\text{exp}}}{30} \times 10^{-0.4 m_*} \right) = m_0, \quad (4)$$

which leads to

$$m_*(n_{\text{psf}}, T_{\text{exp}}) = m_0 + 2.5 \log_{10} \left( \frac{n_{\text{psf}} T_{\text{exp}}}{30} \right), \quad (5)$$

where finally  $m_*$  indicates what must be the maximal magnitude to ensure a 1 per cent level of photometry estimation across the  $40 \text{ arcsec} \times 40 \text{ arcsec}$  field. Table 3 gives the results of equation (5) for the pairs  $(n_{\text{psf}}/T_{\text{exp}})$ . We emphasize that these are empirical results obtained for a NIRC2 baseline with a specific electronic noise configuration, but they highlight that deploying the FPP approach is feasible. We will also consider the near-infrared spectro-imager OSIRIS at Keck II, which has a  $20.4\text{-arcsec}$  FOV imager located at  $19 \text{ arcsec}$  from the spectrograph, which allows us to access strongly anisoplanatism-contaminated PSFs. The next step of this work will consist of coupling FPP with on-axis PSF reconstruction, to be tested on crowded field images.

## 5 APPLICATION TO THE HENOS TESTBED

HeNOS (Herzberg NFIRAOS Optical Simulator) is a multi-conjugated AO test bench designed to be a scaled-down version of NFIRAOS, the first light AO system for the Thirty Meter Telescope (TMT) (Rosensteiner et al. 2016). We used HeNOS in SCAO mode and closed the loop on one of the four LGSs distributed over

**Table 4.** HeNOS set-up summary.

Asterism side length	4.5 arcsec
Source wavelength	670 nm
$r_0$ (670 nm)	0.751
$\theta_0$ (670 nm)	0.854 arcsec
Fractional $r_0$	74.3%, 17.4%, 8.2%
Altitude layer	(0.6, 5.2, 16.3) km
Source height	98.5 km
Telescope diameter	8.13 m
DM actuator pitch	0.813 m

**Table 5.** Strehl ratio and full width at half-maximum measured on HeNOS point spread functions when closing the loop in SCAO mode.

	PSF on-axis	PSF 1	PSF 2	PSF 3
Strehl ratio [%]	28.5	4.0	5.1	4.9
No phase screen	39	41	36	38
FWHM [mas]	21	116	71	100
No phase screen	21	20	21	19

a 4.5-arcsec square constellation, while the atmosphere was created using three phase screens. A summary of the main parameters is given in Table 4. In order to simulate the expected PSF degradation across the field on NFIRAOS at TMT, all altitudes were stretched up by a factor of 11. Moreover, at the time we acquired HeNOS data, the science camera was conjugated at the LGS altitude; LGS beams propagate along a cone but arrive in-focus at the science camera entrance.

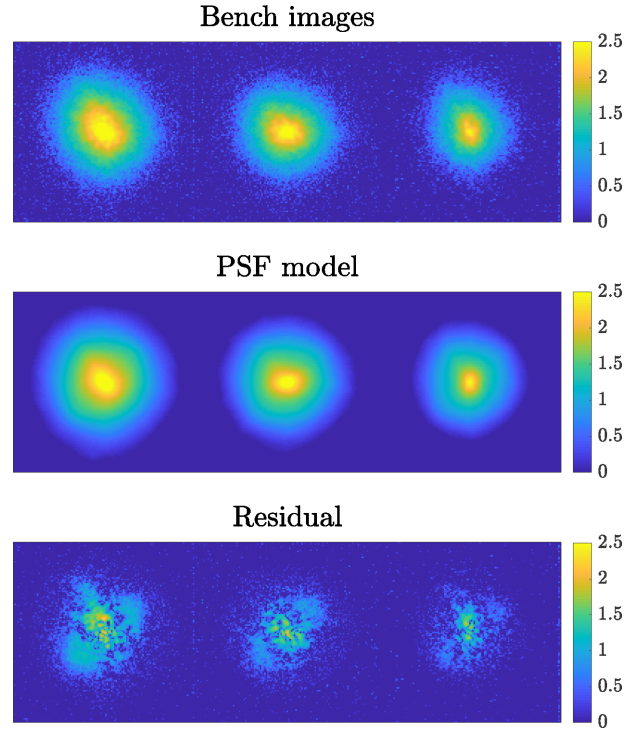
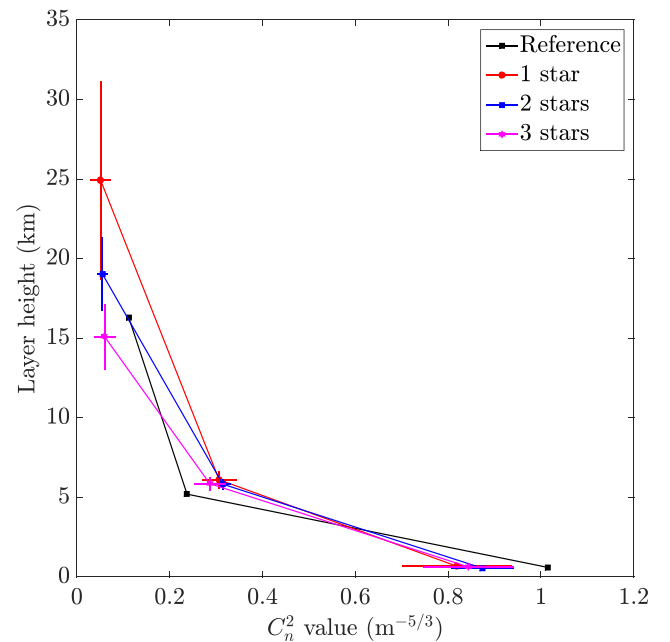
We acquired closed-loop telemetry for guiding the AO system on a LGS in SCAO mode in 2017 July. In addition, we measured PSFs without phase screens through the beam to characterize the best performance in the current set-up. In Table 5 we report the SR and FWHM measurements. On off-axis PSFs, we see that anisoplanatism significantly degrades the performance and dominates any other source of residual errors on off-axis PSFs. This is an ideal situation in which to test the FPP.

$C_n^2(h)$  on the HeNOS bench was estimated using the SLOpes Detection And Ranging (SLODAR) method (Wilson 2002) based on Wave Front Sensor (WFS) cross-correlation, with a 1-km altitude resolution and a measurement precision up to 10 per cent. Consequently, we expect FPP to retrieve a profile very close to the reference given in Table 4, within the measurement accuracy given by the WFS cross-correlation method.

We employed FPP to retrieve both the weights and the heights of three layers by handling one to three stars, providing the reference profile as the initial guess. Fig. 18 illustrates the three off-axis PSFs derived using the three-PSF-based FPP-output profile compared with the observations, which illustrates that our model produces a satisfactory anisoplanatism pattern that matches bench images.

Fig. 19 shows the averaged  $C_n^2(h)$  profile over all PSF pair configurations compared with the reference. Error bars at  $1\sigma$  are deduced from a quadratic mean on the fitting residual given by the minimization procedure and averaged out over PSF pairs (two or three PSFs cases).

First of all, FPP retrieval depends on the number of stars; we see that the single-PSF case does not lead to a successful retrieval when looking at the highest layer, which is significantly overestimated compared with what we expect. This is confirmed in Table 6, which shows that the accuracy on PSF characteristics is worse for the single-star case than using the reference profile as our PSF model

**Figure 18.** (Top) Off-axis HeNOS point spread functions; (middle) best-fitting point spread function (PSF) model using focal-plane profiling; (bottom) fitting residual. Colour bars give the PSF log-scale intensity in digital numbers.**Figure 19.** Retrieved  $C_n^2(h)$  profile compared with the reference value given in Table 4.

inputs. We provide in Table 6 the fraction of variance unexplained (FVU) that derives from the reconstruction residual integrated over all the image, and normalized by the bench mean-free PSF integral as explained in Beltramo-Martin et al. (2018).

The fact that the FPP results depends on the number of reference PSFs is explained by the presence of effects that have not

**Table 6.** Percentage accuracy on outputs retrieved by focal-plane profiling with regard to the number of point spread functions (PSFs). For cases with two and three stars, we averaged the metrics out over all combinations of PSF pairs. Error bars are given at  $1\sigma$ . FVU refers to the fraction of variance unexplained, defined in Beltramo-Martin et al. (2018).

	1 star	2 stars	3 stars	Reference $C_n^2(h)$
FVU	3.5	3.1	3.0	3.2
SR	12.0	6.7	6.5	9.9
FWHM	12.4	11.8	11.6	11.8

been included in the model so far and that are not or are only weakly spatially correlated over the three off-axis PSFs, for example field-dependent static aberrations. These latter effects modify the PSF spatial intensity distribution in the same way as anisoplanatism does, which may confuse the FPP, especially on a single star. A first approach we have to mitigate the unmodelled static phase in the PSF model is to calibrate them, as was done for Keck II (Witzel et al. (2016)). Furthermore, their influence on the retrieval process is diminished by simply collecting more PSFs in the field, illustrated by the present results. In contrast to the anisoplanatism effect, field-dependent features decorrelate spatially and do not necessarily mimic the elongated anisoplanatism pattern on the PSF.

To improve the PSF characterization regarding the FVU metric, the FPP needs at least two reference PSFs to calibrate the profile. For the three-PSFs case, we obtain a  $C_n^2(h)$  estimation that complies with the 10 per cent level precision and 1-km altitude resolution of the WFS-based measurements. Table 6 confirms that this retrieved set of  $C_n^2(h)$  values helps to model the off-axis PSFs more accurately. The difference we see may also be introduced by either anisoplanatism model error – an incorrect stretch factor would make the equivalent asterism different for instance – or a differential conjugation altitude of sources and science camera, which may slightly affect the real  $C_n^2(h)$  as seen in the focal plane compared with the WFS-based identification.

Fig. 19 provides evidence that the retrieved seeing is quite stable and close to the reference value at the 10 per cent level. Furthermore, we notice that only the highest-layer altitude estimation is sensitive to the number of stars. This layer contributes the most to spreading out the PSF, and the FPP tunes the corresponding altitude height to reproduce the FWHM more faithfully.

The next step of this work is to go further in this identification process by collecting more data in closed-loop on different LGSS in order to increase the number of observations. We will be able to pinpoint whether this difference is a real physical effect or just a limitation of our system description. Shifting the real position of phase screens will also provide insights into the FPP altitude resolution.

## 6 CONCLUSION

In this paper we have presented FPP as a  $C_n^2(h)$  retrieval method that relies on partially compensated AO images affected by anisoplanatism. It performs a non-linear least-squares minimization of a PSF model over observations and provides both a PSF model across the field and the  $C_n^2(h)$  profile. In order to mitigate noise propagation and the sensitivity to unmodelled aberrations, such as field-dependent static aberrations, it is necessary to collect several PSFs from the field; we show for the NIRC2 imaging camera at Keck II that the FPP method can retrieve both atmosphere and PSF characteristics at an accuracy level of 1 per cent, as well as photometry and astrometry at an accuracy level of respectively 1 per cent and

50- $\mu$ as if we obtain  $n_{\text{psf}}$  PSFs of magnitude given by  $H = 14 + 2.5 \log(n_{\text{psf}} T_{\text{exp}}/30)$ , which corresponds to  $H = 15.5$  mag for  $n_{\text{psf}} = 4$  and  $T_{\text{exp}} = 30$  s.

We deployed this approach on the HeNOS testbench, where  $C_n^2(h)$  values are measured from WFS cross-correlation. As a result of FPP, we retrieved a profile that complies with WFS-based measurements when using three stars distributed over 4.5 arcsec with  $\theta_0 = 0.854$  arcsec. We demonstrated that collecting more stars leads to the mitigation of model errors such as field-dependent static aberrations.

We focused in this paper on the  $C_n^2(h)$  profiling for the purpose of assessing the reliability and limitations of this method. Our next work will deploy both FPP and a PSF-reconstruction technique to assess the potential gains on crowded field observations, such as the Galactic Centre, with Keck and the ELT with MICADO. Furthermore, we will investigate extending the FPP to tomographic systems to improve the  $C_n^2(h)$  profiling, especially for the purpose of deploying such an approach with the multi-conjugated system MAORY coupled with MICADO, or the laser-tomographic mode of HARMONI and METIS.

## ACKNOWLEDGEMENTS

This work was supported by the A\*MIDEX project (no. ANR-11-IDEX-0001-02) funded by the ‘Investissements d’Avenir’ French Government program, managed by the French National Research Agency (ANR).

## REFERENCES

- Beltramo-Martin O., Correia C., Mieda E., Neichel B., Fusco T., Witzel G., Lu J., Véran J., 2018, *MNRAS*, 478, 4642
- Britton M. C., 2006, *PASP*, 118, 885
- Butterley T., Wilson R. W., Sarazin M., 2006, *MNRAS*, 369, 835
- Conan R., Correia C., 2014, in Adaptive Optics Systems IV of Proc., SPIE, p. 91486C
- Flicker R., 2008, Technical Report, PSF Reconstruction for Keck AO. W.M. Keck Observatory, 65-1120 Mamalahoa Hwy, Kamuela, HI, p. 96743
- Fried D. L., 1982, *J. Opt. Soc. Am. A*, 72, 52
- Fritz T. et al., 2010, *MNRAS*, 401, 1177
- Fusco T., Conan J.-M., Mugnier L. M., Michau V., Rousset G., 2000, *A&A*, 142, 149
- Guesalaga A., Neichel B., Correia C. M., Butterley T., Osborn J., Masciadri E., Fusco T., Sauvage J.-F., 2017, *MNRAS*, 465, 1984
- Helin T., Kindermann S., Lehtonen J., Ramlau R., 2018, *Inverse Problems*, 34, 044002
- Laidlaw D. J. et al., 2016, in Adaptive Optics Systems V of Proc., SPIE, p. 99093I
- Martinez P., Kolb J., Sarazin M., Tokovinin A., 2010, *Messenger*, 141, 5
- Martin O. A. et al., 2016, in Adaptive Optics Systems V of Proc., SPIE, p. 99093P
- McLean I. S., Chaffee F. H., 2000, in Optical and IR Telescope Instrumentation and Detectors of Proc., SPIE, p. 2
- Neichel B., Masciadri E., Guesalaga A. R., Lascaux F., Béchet C., 2014, in Adaptive Optics Systems IV of Proc., SPIE, p. 63
- Ono Y. H., Correia C. M., Andersen D. R., Lardièrre O., Oya S., Akiyama M., Jackson K., Bradley C., 2017, *MNRAS*, 465, 4931
- Osborn J., 2015, *MNRAS*, 446, 1305
- Roddier F., 1999, *Adaptive Optics in Astronomy*. Cambridge Univ. Press, Cambridge
- Rosensteiner M., Turri P., Mieda E., Véran J.-P., Andersen D. R., Herriot G., 2016, in Adaptive Optics Systems V of Proc., SPIE, p. 990949
- Schödel R., 2010, *A&A*, 509, A58
- Tyler G. A., 1994, *J. Opt. Soc. Am. A*, 11, 409
- Véran J.-P., Rigaut F., Maitre H., Rouan D., 1997, *J. Opt. Soc. Am. A*, 14, 3057

Whiteley M. R., Welsh B. M., Roggemann M. C., 1998, in *Adaptive Optical System Technologies of Proc.*, SPIE, p. 177  
Wilson R. W., 2002, *MNRAS*, 337, 103  
Witzel G. et al., 2016, in *Adaptive Optics Systems V of Proc.*, SPIE, p. 99091O

Yelda S., Lu J. R., Ghez A. M., Clarkson W., Anderson J., Do T., Matthews K., 2010, *ApJ*, 725, 331

This paper has been typeset from a  $\text{\TeX}/\text{\LaTeX}$  file prepared by the author.